



Article

Retrieving the Kinematic Process of Repeated-Mining-Induced Landslides by Fusing SAR/InSAR Displacement, Logistic Model, and Probability Integral Method

Hengyi Chen ^{1,2} , Chaoying Zhao ^{1,3,4,*} , Roberto Tomás ² , Liquan Chen ¹ , Chengsheng Yang ¹ and Yuning Zhang ¹

¹ School of Geological Engineering and Geomatics, Chang'an University, Xi'an 710054, China; hychen@chd.edu.cn (H.C.); chenliquan@chd.edu.cn (L.C.); yangchengsheng@chd.edu.cn (C.Y.); 2021126027@chd.edu.cn (Y.Z.)

² Departamento de Ingeniería Civil, Escuela Politécnica Superior de Alicante, Universidad de Alicante, 03080 Alicante, Spain; roberto.tomas@ua.es

³ Key Laboratory of Western China's Mineral Resources and Geological Engineering, Ministry of Education, Xi'an 710054, China

⁴ Key Laboratory of Ecological Geology and Disaster Prevention, Ministry of Natural Resources, Xi'an 710054, China

* Correspondence: cyzhao@chd.edu.cn; Tel.: +86-29-8233-9261

Abstract: The extraction of underground minerals in hilly regions is highly susceptible to landslides, which requires the application of InSAR techniques to monitor the surface displacement. However, repeated mining for multiple coal seams can cause a large displacement beyond the detectable gradient of the traditional InSAR technique, making it difficult to explore the relationship between landslides and subsurface excavations in both temporal and spatial domains. In this study, the Tengqing landslide in Shuicheng, Guizhou, China, was chosen as the study area. Firstly, the large-gradient surface displacement in the line of sight was obtained by the fusion of SAR offset tracking and interferometric phase. Subsequently, a multi-segment logistic model was proposed to simulate the temporal effect induced by repeated mining activities. Next, a simplified probability integral method (SPIM) was utilized to invert the geometry of the mining tunnel and separate the displacement of the mining subsidence and landslide. Finally, the subsurface mining parameters and in situ investigation were carried out to assess the impact of mining and precipitation on the kinematic process of Tengqing landslides. Results showed that the repeated mining activities in Tengqing can not only cause land subsidence and rock avalanches at the top of the mountain, but also accelerate the landslide displacement. The technical approach presented in this study can provide new insights for monitoring and modeling the effects of repeated mining-induced landslides in mountainous areas.



Citation: Chen, H.; Zhao, C.; Tomás, R.; Chen, L.; Yang, C.; Zhang, Y. Retrieving the Kinematic Process of Repeated-Mining-Induced Landslides by Fusing SAR/InSAR Displacement, Logistic Model, and Probability Integral Method. *Remote Sens.* **2023**, *15*, 3145. <https://doi.org/10.3390/rs15123145>

Academic Editor: Michele Saroli

Received: 17 May 2023

Revised: 5 June 2023

Accepted: 14 June 2023

Published: 16 June 2023



Copyright: © 2023 by the authors. Licensee MDPI, Basel, Switzerland. This article is an open access article distributed under the terms and conditions of the Creative Commons Attribution (CC BY) license (<https://creativecommons.org/licenses/by/4.0/>).

1. Introduction

Mining activities have been responsible for numerous catastrophic landslides globally, leading to substantial damage to properties and loss of lives. The extraction of underground minerals induces bending and breakage of the overlying rock strata, resulting in tension cracks, ground settling, and severe landslides in mountainous regions. For instance, on 5 June 2009, the Jiweishan landslide that occurred in Chongqing, China resulted in 74 deaths [1,2]. On 10 April 2013, the Bingham Canyon landslide that occurred in Salt Lake City, Utah, USA caused extensive damage to property and infrastructure [3,4]. Similarly, on 28 August 2017, a landslide in Nayong County, China, resulted in 26 fatalities [5], while on 2 July 2020, a landslide at the Hpakant Jade Mine in Myanmar killed at least 172 miners [6]. These incidents serve as a clear indication of the landslide hazards related

to mining operations and emphasize the need for efficient monitoring and analysis of landslide displacement to reduce the risks of such calamities.

Interferometric Synthetic Aperture Radar (InSAR) is one of the efficient tools to retrieve surface displacements with large coverage and high-precision ranging from centimeters to millimeters [7,8]. Once the phase information of persistent scatterers or distributed scatterers has been extracted, the displacement time series can be obtained through the multi-temporal InSAR methods [9,10]. Among them, the typical small baseline subsets (SBAs) approach can suppress the decorrelation effect based on optimizing the combination of interferometric pairs with a short spatiotemporal baseline [11]. These advanced InSAR methods have made great contributions to monitor the mining subsidence or landslide displacement [12–15], detect the potential active landslides [16,17], or dynamically estimate the deformation parameters [18,19]. However, mining operation in hilly regions can cause significant landslide events characterized by steep displacement gradients [2,5]. Once the surface displacement exceeds the detectable gradient of InSAR, it may only be able to capture the margin of the displacement field [20]. Nevertheless, the offset tracking algorithm (OFT) can be employed successfully to obtain the large-gradient displacement based on the principle of cross-correlation patch matching [21,22]. Nevertheless, the accuracy of OFT is lower compared with InSAR, as it is primarily dependent on the image resolution size and the precision of registration [22]. Therefore, some studies have combined the advantages of both techniques by using coherence coefficients to fuse phase-based and amplitude-offset-based displacements [23–25].

On the other hand, some studies have been carried out to explore the failure mechanism of landslides caused by underground mining extraction, such as the influence function methods [26], physical tests [27,28], and numerical simulations [29,30]. However, due to the kinematic process of mining-related landslides encompassing both mining-induced subsidence and slope instability, limited research has been conducted to separate the spatiotemporal interaction between landslides and subsurface excavation. As mining activities are carried out through regular working faces, it is possible to simulate the deformation process of mining activities and invert the subsurface mining parameters based on mining models and surface displacement, which is subsequently beneficial for exploring the disaster factors and the impact extent of mining-related landslides.

In the temporal domain, the mining-induced surface displacement typically exhibits S-shaped curves, which represent the displacement stages of initiation, acceleration, deceleration, and suspension. Accordingly, the logistic time function is capable of simulating mining subsidence [31,32] and is therefore suitable for assessing the mining contribution to landslide hazards in the temporal domain [33,34]. Moreover, it is often required to repeat the mining process many times to achieve the full utilization of resources, leading to periodic surface displacements associated with the repeated mining cycles [35–37]. To address this issue, a multi-segment logistic model is proposed in this study, which combines the segmentation function with the logistic model to simulate repeated-mining-induced surface displacement.

In the spatial domain, the source parameters can be inverted once the relationship between geodetic observation and models is built, such as the magma reservoir of volcanoes [38], the fault geometry of earthquakes [39], or the hydrogeology parameters of aquifer storage [40]. Similarly, the mining-induced surface displacement can usually be modeled by the probability integral method (PIM) through setting a series of relevant mining parameters [41,42]. Conversely, the parameters of the mining galleries can be subsequently inverted once the surface displacement is known [43,44]. Therefore, the spatial effect caused by mining activities is modeled by the PIM, and the displacement field of the mining subsidence and sliding surface can be separated accordingly.

In this paper, Tengqing landslides are selected as the study area and they are the typical mining-related landslides that are located in Shuicheng County of China. Since the operation of the Tengqing coal plant in 2016, multiple landslide events have occurred in this place. Because of the complex monitoring conditions and the severe damage, the

kinematic process of Tengqing landslides is still unclear, and the relationship between the subsurface repeated mining and slope failure remains unknown.

Therefore, the manuscript is organized as follows. In Section 2, we will introduce the background about the Tengqing landslides and the relevant research datasets. In Section 3, we will provide a fusion displacement monitoring method based on phase and amplitude SAR images, along with two mining models. In Section 4, we will show the main results. In Section 5, we will discuss the kinematic process and disaster factors of repeated-mining-induced landslides. In Section 6, we will provide the final conclusion of this work.

2. Study Area

Figure 1a indicates the geographical location of the Tengqing landslides. This place is located in Nayong County, China, and presents a fragile karst landform with steep terrain. Since the Tengqing coal mine was put into production in 2016, many landslide events have occurred near the mine site, which caused the nearby residents to be moved before October 2017.

In fact, there are two mountains that are located in the north central and southeastern parts of the mining facility, as shown in Figure 1b,c. The first mountain has a maximum elevation of 1873 m a.s.l. and is known as Heilingjing (referred to as HL hereafter). The second mountain, with a maximum elevation of 1950 m a.s.l., is called Fenghuangshan (referred to as FH hereafter). Figure 1c presents the geological structure of the Tengqing landslides. The stratigraphic orientation is approximately in the north–south direction, and the dip is nearly 12–25°.

As the geological cross-section shown in Figure 1e, the main outcrops and the distribution of rock formations are organized as follows: (1) The Lower Triassic Yelang Formation (T_1y) is distributed at the summit of the mountain. It is dominated by hard rocks, mainly containing gray medium-thick tuff, while the cliff area includes siltstone, shale, and mudstone. (2) Following this are the Upper Permian Changxing and Dalong Formations ($P_2c + d$), which are about 54 m thick and consist mainly of gray limestone interspersed with shale, sandy shale, and claystone. (3) The stratum of the Permian Upper Longtan Formation (P_2l) mainly contains mudstone and coal seams. (4) The underlying stratigraphy belongs to the Permian Upper Emeishan Basalt ($P_2\beta$). In summary, the upper layers of rock in this area are hard and steeply inclined, while the lower layers are softer and have a gentler slope.

There are eight coal seams stored in stratum P_2l that can be mined out. The long wall mining and total collapse method are conducted for exploitation and roof management. According to the mining plan of the Tengqing mining factory, the planned extraction distance along the strike is 1100 m, and approximately 400 m along the dip direction. The elevation of the mining operation is from 1160 to 1750 m a.s.l., and the average value of the mining depth is nearly 570 m. The sum of the thickness of all mineable seams is approximately 12.81 m and the average dip angle is about 15°.

Figure 1d is the UAV image of Tengqing landslides, and the large cracks and broken cliff of the mountain pose a serious threat to the surrounding roads and villages. Repeated mining extraction can lead to an imbalance of rock layers, resulting in ground rupture, collapse, and the potential occurrence of severe rock avalanches or landslides. Figure 2 shows the optical images of Google Earth and China Map-World from 2014 to 2020. Before 2014, there were no apparent changes in the Tengqing mining site and the surrounding mountains. However, some of the slopes underwent landslides after 2017. From 2018 to 2020, the number of landslides as well as their impact area further expanded. The road at the front of the slope was damaged and the village was relocated. Due to the large topographic relief and frequent mining activities, especially in the location of mountain FH, tension cracks have appeared on the top of the mountain. Furthermore, the rock layers at the cliff have gradually become fractured, scraping the slope surface and increasing the occurrence of landslides. Therefore, it is crucial to retrieve the surface displacement of

Tengqing landslides and explore the dynamic processes of mountain subsidence and slope instability.

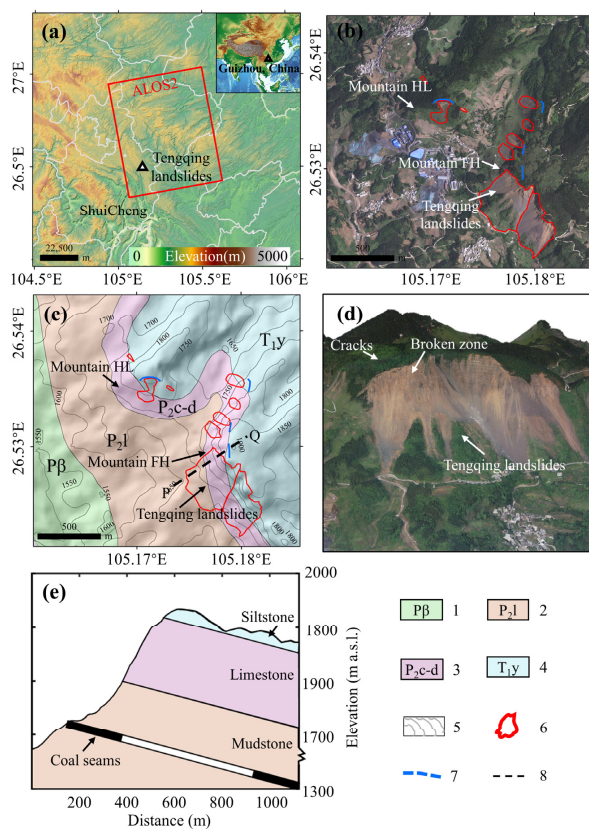


Figure 1. (a) Geographical location of Tengqing landslides and coverage of ALOS/PALSAR-2 images (red rectangle). (b) Optical image. (c) Geological map. (d) UAV image of Tengqing landslides. (e) Cross-section from point P to Q. The legends are organized as follows: 1. Emeishan basalt Formation of Upper Permian System; 2. Longtan Formation of Upper Permian System; 3. Changxing and Dalong Formation of Upper Permian System; 4. Yelang Formation of Lower Triassic System; 5. Contours at 50 m intervals; 6. Historical landslides; 7. Visible Cracks; 8. Profile P-Q.

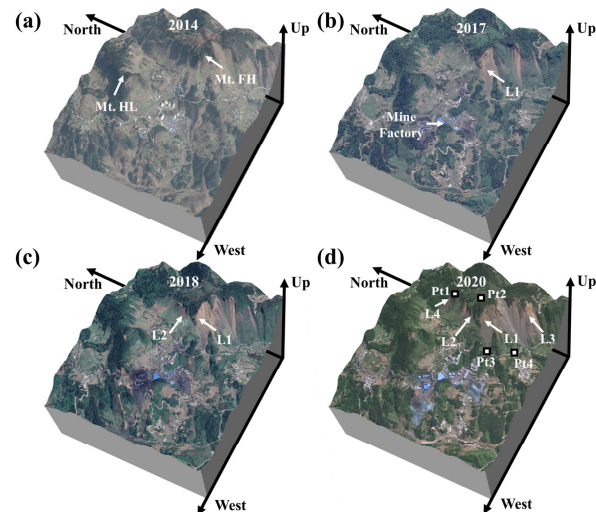


Figure 2. Three-dimensional digital terrain models of Tengqing landslides from different periods. L1, L2, L3, and L4 represent the landslide events that occurred at different stages. Tensile cracks were found at the location of points Pt1 and Pt2, while points Pt3 and Pt4 represent water outlets. (a–d) indicate the increase of landslide events after mining operations.

3. Data and Methods

3.1. Data

To monitor the surface displacement of Tengqing landslides and mitigate the decorrelation effect of dense vegetation, we acquire 18 L-band ALOS/PALSAR-2 (ALOS2) images, covering the time period from May 2017 to September 2021. The incidence angle of ALOS2 datasets is about 39° and the flight direction is in ascending orbits. In addition, the topographic phase is estimated by 30 m SRTM. The optical images, acquired from Google Maps and China Map-World, are used to investigate the instability of the slope. In order to analyze the rainfall effect, the daily global precipitation measurements (GPMs) are used.

3.2. Methods

Figure 3 shows the methodology utilized in this study, including the calculation of the large-gradient displacement field by fusing SAR/InSAR methods, the simulation of the deformation process by the multi-segment logistic model, and the inversion of mining geometry based on the SPIM.

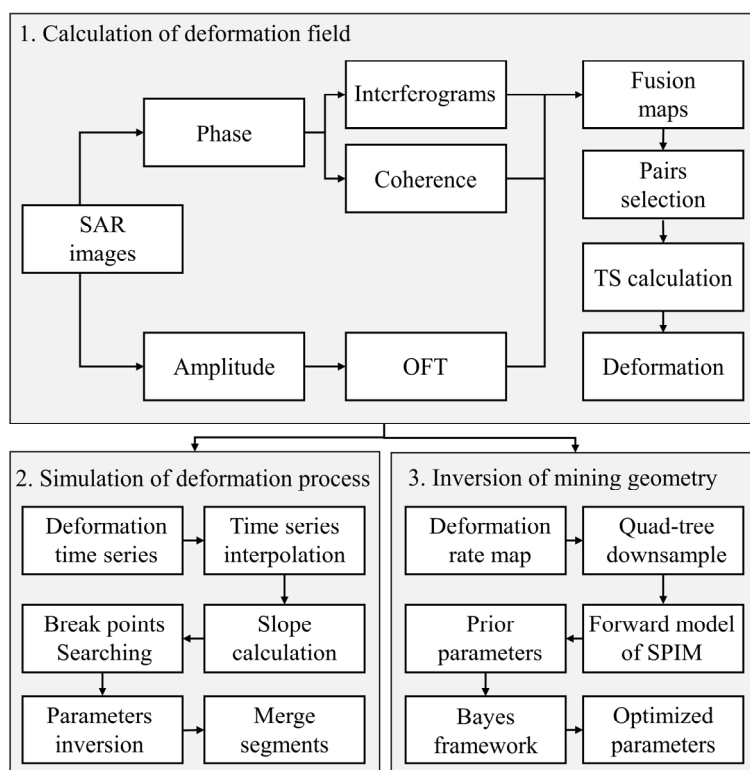


Figure 3. General flowchart for monitoring and analysis of the deformation processes of landslide induced by repeated mining.

3.2.1. Coherence-Guide Fusion of InSAR and SAR Offset Tracking

Because InSAR technology is applicable to the small-gradient displacements, and the OFT method is more sensitive to large-gradient displacements [21,22,45], this study utilizes the coherence-guide method to fuse phase-based and amplitude-offset-based displacements. For comparison, the SBAS method is also utilized to monitor the surface displacement.

The multi-look ratio and the offset search step in range and azimuth are both 2 to 2. The differential interferogram is filtered using a window size of 16×16 and the offset tracking uses a window size of 128×128 . In some cases, ALOS2 images may have long time intervals between adjacent pairs, leading to temporal decoherence and poor interferometric effects. Therefore, the selection of interferometric pair combinations for both the SBAS and fusion algorithms depends on empirical considerations. For the SBAS, we reject interferograms only if the deformation region is completely contaminated by

noise. For the fusion method, we retain only the interferograms with small displacement magnitudes in the displacement region and select the rest according to the fusion quality. The spatiotemporal baseline configuration of the SBAS and fusion method is shown in Figure 4.

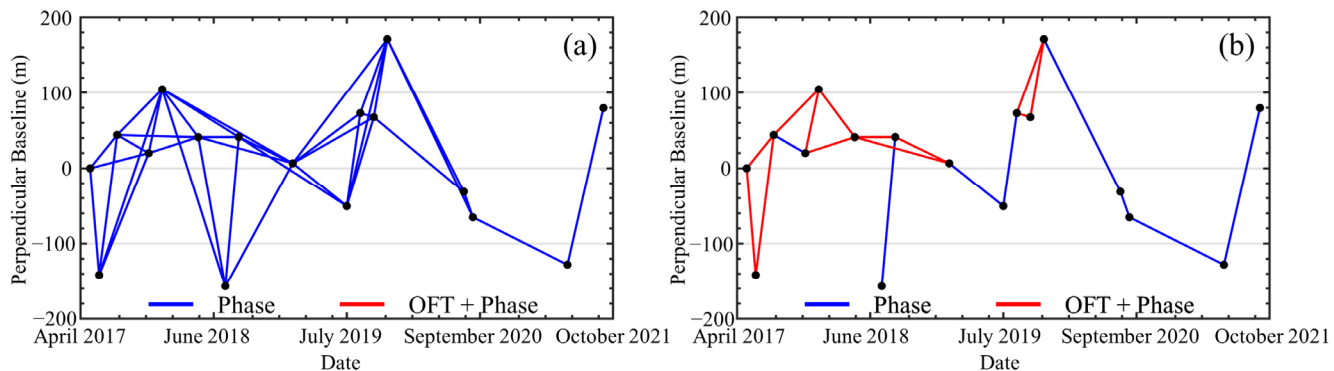


Figure 4. Spatial and temporal configuration of SBAS (a) and the fusion method (b).

The coherence coefficient threshold is set to 0.5 as an indicator for fusing the combined pairs. Point targets with coherence values below the threshold are substituted with the offset tracking results, whereas those with values above the threshold are maintained with their original unwrapped differential interferometric phase. Moreover, interferograms exhibiting small displacement gradients are directly employed in the final time series inversion without the fusion processing.

3.2.2. Multiple-Segment Logistic Model

The surface displacement of mining subsidence would usually show an S-shaped process of “initiation-acceleration-deceleration-suspension”, and the logistic time function can be used to describe this process [31,32,34]. The equation is as follows (1):

$$W(t) = W_0 / (1 + ae^{-bt}) \quad (1)$$

where t represents the given time, $W(t)$ is the predicted displacement, and W_0 is the maximum displacement. If $t_0 = 0$, $W(t_0) = 0$. A and b are used to control the shape of the displacement time series.

However, the surface displacement caused by repeated mining activities often shows multiple S-shaped periods [35,36], and only a single model is not sufficient to simulate this characteristic. Nevertheless, it can be achieved through the combination of the segmentation function and logistic model, as shown in next equation:

$$W(t_{si}) = W_{0s1} / (1 + a_{s1}e^{-b_{s1}t_{s1}}) + W_{0s2} / (1 + a_{s2}e^{-b_{s2}t_{s2}}) + \dots + W_{0si} / (1 + a_{si}e^{-b_{si}t_{si}}) \quad (2)$$

where subscript si ($i = 1, 2, 3 \dots n$) indicates the number of each segment, $W(t_{si})$ is the predicted displacement of the given time t_{si} , and $W(t_{si})$ is the maximum displacement of the i -th segment. a_{si} and b_{si} are the shape parameters at the i -th segment.

With the increase in segments, the function tends to be more complex and the inversion of the model parameters becomes more complicated. For example, if there are four segments, 12 parameters will have to be inverted. In response to this problem, the prerequisite is to distinguish the time boundaries of each segment. Figure 5 represents the diagram of the multi-segment logistic model, and the black dashed and solid lines represent the simulated displacement time series and its instantaneous velocity, respectively. The instantaneous velocity changes from monotonically decreasing to monotonically increasing at the boundary of each segment. Thus, the boundary of each segment can be determined by detecting the position of each local maximum peak in the instantaneous velocity. Local peak points in Figure 5 indicate the locations with the maximum values within the respec-

tive segments, which are used to split the displacement time series into multiple segments for logistic curve modeling. To reduce the likelihood of detecting spurious or insignificant peaks in the signal, a threshold of peak prominence is set, below which peaks are excluded from the analysis [46]. Subsequently, the nonlinear least-squares regression is performed to invert the model parameters. Additionally, if the displacement during a certain period is not apparent, we will exclude it from the parameter inversion process.

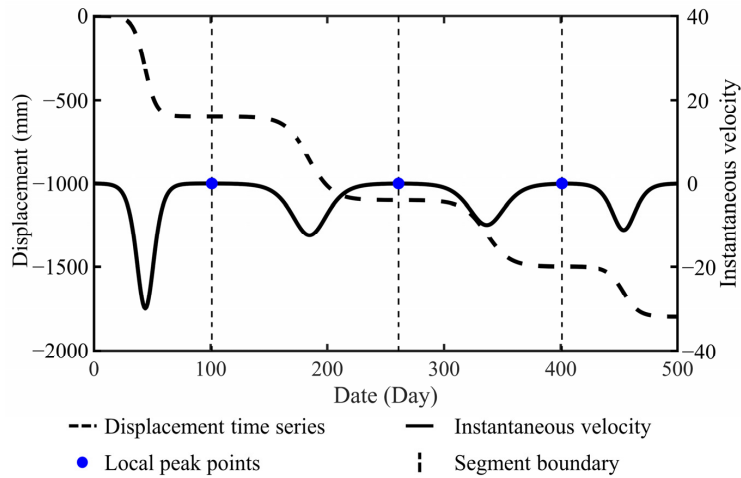


Figure 5. Diagram of the multi-segment logistic model.

In summary, we split the deformation process of repetitive monitoring into separated segments and then invert the parameters individually. All segments are finally combined to restore the overall deformation process. Moreover, based on the monitored displacement time series and simulated results of the proposed multi-segment logistic model, the comparison of the maximum subsidence or shape parameters can help assess the impact of disaster factors, including repeated mining activities and rainfall.

3.2.3. Probability Integral Method

Figure 6 is the geometrical representation of the PIM. The bottom map is the mining surface, while the top map indicates the predicted surface displacement through the given parameters of the mining tunnel. In the local coordinate system (S, O_M, D) , S and D represent the strike and dip directions of the mining tunnel, respectively, and O_M is the central point of the working face, which has the same geographical coordinate system as point O_G of the ground surface.

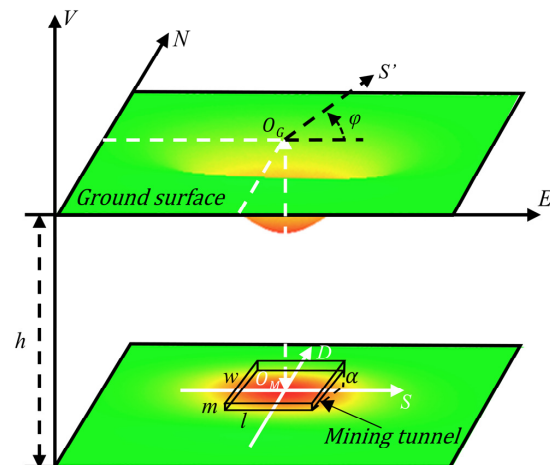


Figure 6. Geometrical representation of the Probability Integral Method. The green area represents the stable area and the red area represents the deformation field caused by mining activities.

Based on previous research on the PIM [43], we adjust some of the equations and divide the inversion process of optimal parameters into the following three steps: (1) The initial parameters and the upper and lower bound are set according to the prior information, and the surface displacements in the vertical, strike, and dip directions are modeled. (2) The displacement field in the strike and dip direction of the mining tunnel are then converted to east–west and north–south directions of the geographic coordinate system. (3) The LOS displacement is calculated through the three-dimensional displacement, and the residual between the original and modeled LOS displacement field is used to guide the modification of the inversion steps.

If the parameters of the underground mining tunnel are given, the corresponding surface displacement in the vertical d_V , strike d_S , and dip d_D directions at point (x, y) can be predicted as Equation (3):

$$\begin{cases} d_V(x, y) = W(x)W(y)/W_0 \\ d_S(x, y) = U(x)W(y)/W_0 \\ d_D(x, y) = U(y)W(x)/W_0 \end{cases} \quad (3)$$

in which $W_0 = m \cdot q \cdot \cos\alpha$, $L_1 = l - 2s_3$, $L_2 = ((w - s_1 - s_2) \cdot \sin(\theta_0 + \alpha))W_0$, $\text{erf}(x) = (2/\sqrt{\pi}) \cdot \int_0^x \exp(-u^2)du$, $W(x) = W_0(\text{erf}(\sqrt{\pi} \cdot \tan\beta \cdot x/h) - \text{erf}(\sqrt{\pi} \cdot \tan\beta \cdot (x - L_1)/h))/2$, $W(y) = W_0(\text{erf}(\sqrt{\pi} \cdot \tan\beta \cdot y/h) - \text{erf}(\sqrt{\pi} \cdot \tan\beta \cdot (y - L_2)/h))/2$, $U(x) = b \cdot W_0(\exp(-\pi \cdot \tan\beta^2 \cdot x^2/h^2) - \exp(-\pi \cdot \tan\beta^2 \cdot (x - L_1)^2/h^2))$, and $U(y) = b \cdot W_0(\exp(-\pi \cdot \tan\beta^2 \cdot y^2/h^2) - \exp(-\pi \cdot \tan\beta^2 \cdot (y - L_2)^2/h^2)) - \cot\theta_0 \cdot W(y)$.

The relevant geometry parameters of the PIM include the geographic coordinates of the central point $O_G(C_{lon}, C_{lat})$, length l , width w , thickness m , dip angle α , and mining depths h . In addition, there are also some prior parameters, including the subsidence factor q , horizontal displacement constant b , angle of major influence β , propagation angle of mining θ_0 , and the offsets of the inflection points in the two strike direction sides s_3, s_4 and two dip direction sides s_1, s_2 of the goaf. The empirical parameters can be set based on the prior information and similar geological conditions [43].

To further build the forward model between surface displacement in the line-of-sight (LOS) direction and mining parameters, the horizontal displacement in the local mining coordinate system should be converted into the geographical coordinate system.

$$\begin{cases} d_{EW} = d_S \cos \varphi - d_D \sin \varphi \\ d_{NS} = d_S \sin \varphi + d_D \cos \varphi \end{cases} \quad (4)$$

As expressed in Equation (4), φ represents the counterclockwise rotation angle from the eastward direction to the strike direction of the mining tunnel. When $\varphi = 0$, the horizontal displacement in the east–west d_{EW} or north–south d_{NS} direction is the same as it is in the strike or dip direction, respectively. If $\varphi \neq 0$, the displacement in the strike and dip direction should be converted to the geographical coordinate system. After that, according to the incidence angle θ and flight direction α_h of the SAR satellite, the displacement in the LOS direction can be calculated as $d_{LOS} = [d_V, d_{EW}, d_{NS}] * [\cos\theta, -\sin\theta \cdot \sin(\alpha_h - 3\pi/2), -\sin\theta \cdot \cos(\alpha_h - 3\pi/2)]^T$. Subsequently, optimal parameters are inverted by the non-linear least squares method in cooperation with the Levenberg–Marquardt algorithm. Finally, the spatial effect of mining activities is modeled and split from the original deformation field; thus, the effects of mining and landslides are separated for further analysis.

4. Results

The annual displacement rate maps are obtained by SBAS and the fusion methods, respectively. As shown in Figure 7, the SBAS method only captures part of the displacement field. In contrast, the large-gradient displacement of the entire slope in the LOS direction is

successfully retrieved by the fusion method. As a result, the coverage of the displacement field increases by approximately 464,779 m².

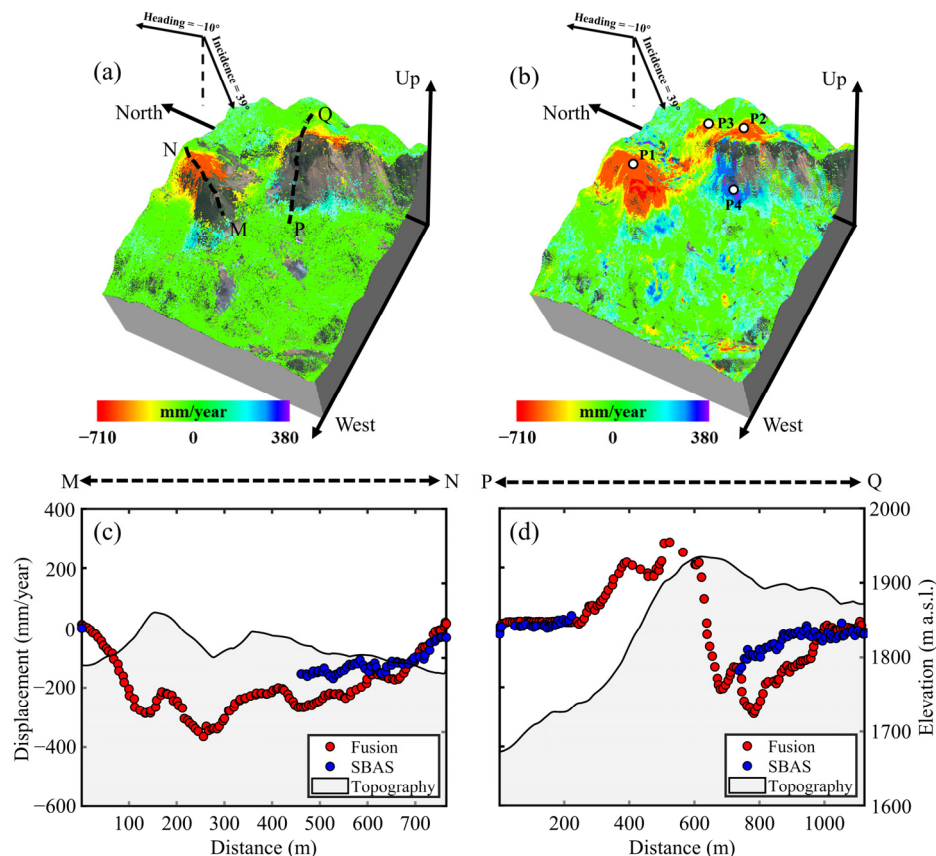


Figure 7. Annual LOS displacement rate maps of Tengqing landslides derived by the SBAS-InSAR (a) and the fusion method (b). (c,d) is the displacement profiles along M-N and P-Q, respectively. P1–P4 represent the typical points selected from displacement field, which will be used to extract the displacement time series for subsequent analysis.

Furthermore, to compare the results of the two methods, we extract two displacement profiles, namely M-N and P-Q, as illustrated in Figure 7c,d, respectively. The fusion method yields a greater magnitude of displacement compared to the SBAS method. In addition, there is a notable distinction between the SBAS method and the fusion method. The calculation of annual displacement rates by the SBAS method primarily relies on differential interferograms, whereas the fusion method incorporates an SAR-amplitude-based pixel offset to capture large-gradient displacements. Due to the unwrapping error at the large-gradient displacements region by only using phase measurement, the deformation rate derived from the SBAS method is possibly smaller than the fusion results, as shown in Figure 7c,d. The fusion method not only captures displacements in areas where phase monitoring cannot obtain sufficient monitoring points, but it also retrieves large-gradient displacements.

In addition, as shown in Figure 7b, both mountain HL and mountain FH exhibit significant displacements. Notably, landslide-related displacements are apparent in mountain FH. Moreover, the displacement gradient of mountain HL is much greater than that of mountain FH, and the maximum displacement rate is about −710 mm/year. Additionally, as shown in Figure 7c,d, the greater height difference and steep topography of the cliff, along with the fragile rock structure, make mountain FH highly susceptible to collapse and toppling due to mining activities. To our current knowledge, the movement type of the Tengqing landslides can be classified as toppling landslides, where the rock at the top of the slope breaks and separates from the parent body, eventually causing the rock avalanche.

In particular, the negative displacements are concentrated at the summit of mountain FH, and the slope displacements exhibit positive values. Based on the incidence angle shown in Figure 7a, the displacement direction of the slope is toward the LOS direction of the ascending SAR satellite. If the displacement toward the west direction is greater than that of the vertical downward direction, it will be easily prone to this anomalous phenomenon [47–50].

To further explore the kinematic process of Tengqing landslides, we extract the displacement time series from four typical points, which are mainly located at the center of the displacement patterns in Figure 7b. The original displacement time series is represented by the red points in Figure 8(a1–d1). The observation points indicated by red dots represent the monitored displacement time series based on the fusion method. Moreover, we straightforwardly convert the value of point P4 to negative signs to facilitate comparisons with other displacement results easier.

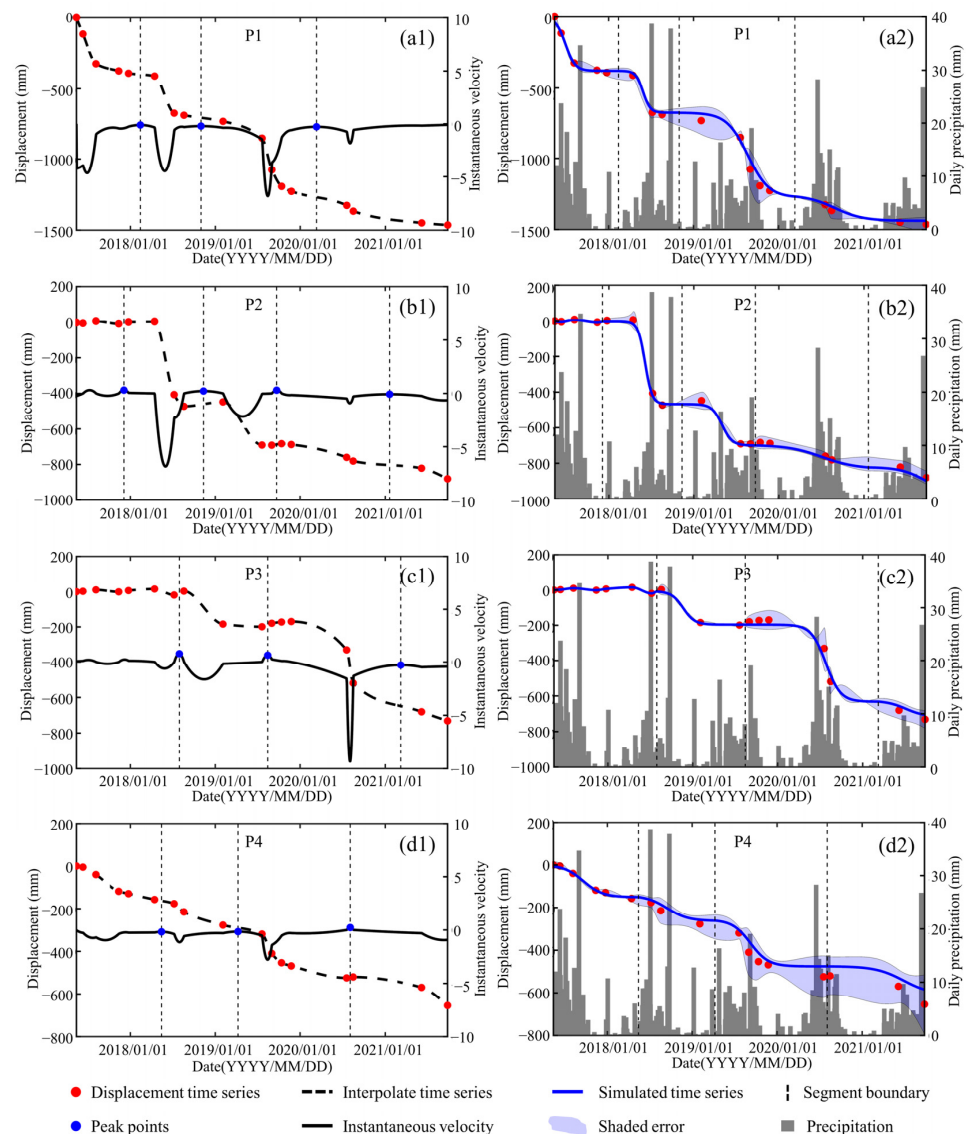


Figure 8. Displacement and rainfall time series of Tengqing landslides. (a1–d1) Original and interpolated displacement time series of four typical points. (a2–d2) Temporal modeling results of displacement time series by the multi-segment logistic model. The signs of the displacement time series at point P4 are inverted to negative values to facilitate comparison with other displacement results.

The displacement time series presents multiple periods, with each period containing an “initiation-acceleration-deceleration-suspension” stage. Mining tunnels are designed according to the spatial storage and construction conditions of resources, and it can be used to guide the extraction and retraction of the coal resources. As there are multiple layers of coal seams stored underground, repeated mining is required. After the first extraction, the bedrock above the mining tunnel tends to bend and then cause surface subsidence. Additionally, the repeated excavation can cause periodic roof collapses, which leads to the displacement time series to present multiple S-shaped segments. Furthermore, the initiation time of surface deformation at different locations is not the same, and this is related to the varying start times of mining activities.

5. Discussion

5.1. The Temporal Simulation of the Deformation Process

To explore the temporal impact of repeated mining activities and other disaster factors on the Tengqing landslide, we utilize the multi-segment logistic model to simulate the deformation process induced by repeated-mining activities. This can also be beneficial for analyzing the effects of other disaster factors by isolating the mining effect in the temporal domain. The discrete and sparse time series are interpolated as the black-dashed lines in Figure 8(a1–d1). The boundaries of each segment are determined by calculating the instantaneous velocity and detecting local peak points. A peak prominence threshold is set to 0.5 to ensure accurate peak detection and avoid detecting wrong peaks. The simulation results of the multi-segment logistic model are shown in Figure 8(a2–d2) and the blue shaded error represents the range of deviation between the simulation results and the interpolated displacement time series. The maximum subsidence for each segment is listed in Table 1.

Table 1. Inverted maximum subsidence of each segment using the multi-segment logistic model. The zero indicates no observable displacement during that period.

Points	Segments				
	$W0_{s1}$	$W0_{s2}$	$W0_{s3}$	$W0_{s4}$	$W0_{s5}$
P1	-379	-296	-600	-180	0
P2	0	-465	-232	-134	-144
P3	0	-189	-435	-89	0
P4	-151	-119	-218	-133	0

The simulated results present a general consistency with the observed displacement time series. The vertical gray dashed boundary lines indicate that the entire observation period consists of 3 or 4 segments. Figure 8(a2) and Table 1 show that the displacement of point P1 reached its maximum subsidence value during the last mining segment, and the displacement tends to be stabilized. This indicates that the mining activities beneath the mountain HL have gradually stopped. However, Figure 8(b2,c2) shows that the mountain FH is still undergoing continuous displacement and has not yet reached its maximum subsidence value during the last segment. This underscores the importance of ongoing monitoring to fully understand the extent and potential influence on the mountain and the surrounding area from mining activities. In addition, the different behavior of displacement between mountain HL and FH may relate to the different slopes and geological conditions. Due to the fragile karst landforms in the study area, the steep terrain of the mountainous FH slope is particularly susceptible to deformation, which can further exacerbate the instability.

Nevertheless, Figure 8(d2) shows that there is a discrepancy between the simulated mining displacement and the observation values. This deviation may be caused by model errors and the influence of rainfall. Additionally, as P2 and P4 are spatially close, the displacement trend should be similar. During the initial segment, while point P2 remained stable, displacement had already taken place at point P4. In the subsequent segments, the

magnitude and velocity of the displacement at point P4 do not significantly increase during the acceleration stage of point P2.

In addition, according to the comparison of daily precipitation and the deformation process in Figure 8(a2–d2), there is no obvious correlation between rainfall and the displacement of points P1 to P3. However, it shows a noticeable acceleration trend at point P4 during the rainy season from 2017 to 2019. This trend results in an increasing discrepancy between the model values and the monitored results. In addition, a field survey was performed in October 2020, and Figure 9 displays the corresponding in situ photographs. The positions of the four photographs are labeled in Figure 2d with white rectangles bordered in black. A number of tension cracks are developed in the crown of the landslide. The largest one, shown in Figure 9b, reaches 47 m in length and 0.2 m in width. Rainfall can seep into these tension cracks and penetrate through the fractures and karst pipelines. This infiltration can result in increased erosion of the rock mass, which in turn accelerates the slope displacement [5]. Furthermore, two natural outlets are identified at the base of the mountain, which further confirms the internal hydrogeological effects on slope displacement.

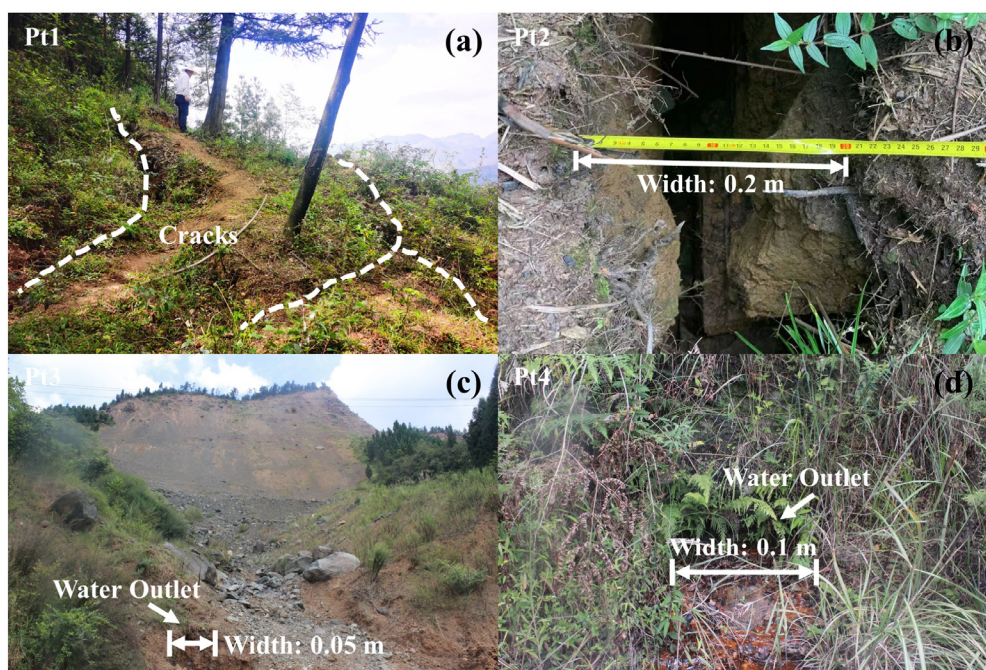


Figure 9. In situ photos of Tengqing landslides, including the tension cracks (a,b) and the outlet of karst water (c,d).

5.2. The Spatial Separation of Mining and Landslide Deformation Field

The temporal simulation of the deformation process of the Tengqing landslide indicates that mining activities had a substantial effect on slope instability. To highlight the effects of mining on landslides in the spatial domain, the optimal mining parameters are inverted by the SPIM and fusion results. Accordingly, the three-dimensional and LOS displacement fields caused by mining activities are modeled. The original deformation field is subsequently separated into mining subsidence and sliding surface.

Underground mining activities in mountain FH involve multiple small-scale working faces that operate at different periods and locations, making it challenging to model the irregular displacement field caused by repeated mining. To simplify the inversion process, we assume the original displacement field is induced by a single integrated working face and use the average annual displacement rate to estimate the mining parameters. Considering prior information including Tengqing mining reports and geological conditions, we set $q = 0.83$, $b = 0.34$, $\tan\beta = 1.72$, $s_1 = s_2 = s_3 = s_4 = 5.3$, and $\theta_0 = 79.8$. In addition, the

slope displacement is masked during the inversion process to isolate its influence, and the optimal parameters are listed in Table 2.

Table 2. Mining parameters derived by fusion results and SPIM.

Parameters	Length (m)	Width (m)	Depth (m)	Thickness (m)	Dip (°)	Rotation Angle (°)	Lon (°)	Lat (°)
Model	413.6	141.5	542.9	1.1	15.1	95.7	105.177	26.534

Figure 10a–c represent the original, modeled, and residual displacement fields in the LOS view, respectively, and Figure 10d–f represent the three-dimensional displacement field. The positive values in Figure 10e,f represent the displacement toward the east or north directions, respectively, while the negative values represent the opposite direction. The geographical location of the modeled mining tunnel is calculated according to the inverted parameters, as the black rectangles present in Figure 10.

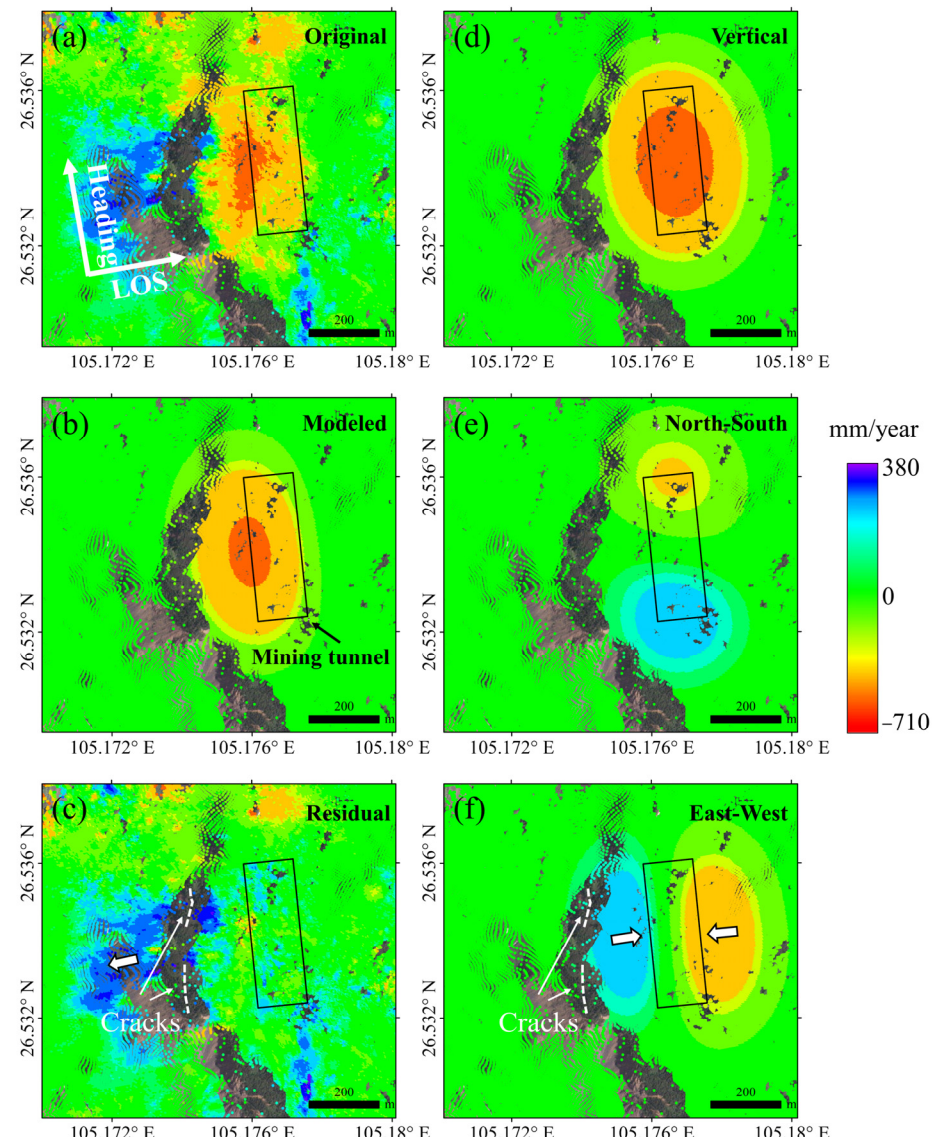


Figure 10. Displacement maps of original and modeled results using the SPIM of mountain FH. (a–c) The original, modeled, and Residual deformation field in LOS view, respectively. (d–f) The components of displacement field in the three-dimensional direction. The black rectangles in (a–f) represent the spatial location of modeled mining tunnel. The arrows in (c,f) with black borders and white interior represent the rough direction of the local horizontal displacement.

Although the simulated displacement field in Figure 10b is relatively regular, the overall simulation results are acceptable, and the residual displacement in Figure 10c is mainly concentrated in the slope. Moreover, the modeled integrated mining tunnel has a length of 413.6 m, a width of 141.5 m, and a depth of 542.9 m. The thickness of the extracted coal seams is about 1.1 m and the dip angle is 15.1°. The rotation angle of the mining tunnel relative to the eastern direction is approximately 95.7°. According to the mining plan in Tengqing, the average depth is nearly 570 m and the average dip angle is about 15°, which proves that the inversion results are similar to the actual mining activities.

The excavation of coal seams can cause the upper rock layer of the mining tunnel to lose the support and tend to bend, which can further cause the sinking of the summit [29]. In addition, Figure 10e,f show that the horizontal displacement of mining subsidence is oriented toward its center. Especially, the eastward displacement induced by mining activities in Figure 10f is opposite to the sliding direction of the slope. This uneven surface displacement is highly susceptible to forming tensile cracks at the crown of the slope [27,51]. Furthermore, intense rainfall also plays a crucial role in slope deformation, as it can infiltrate the rock mass through ground fissures and rock fractures, softening the rock layer and increasing the load on the slope.

5.3. The Formation Process of Mining-Induced Landslides

The Tengqing landslide is located in a typical karst mountain area with fragile geological and hydrological conditions. The strata at the top of the mountain are hard carbonate formations, while the lower strata are relatively soft. The terrain is steeper at the top than at the bottom, making this geological feature prone to large rock avalanches. In addition, the substantial rainfall in this place leads to the long-term dissolution of the upper carbonate surfaces and the creation of intricate karst pipeline systems. Consequently, the infiltration of karstic water exacerbates the erosion process and undermines the stability of the slope structure. Furthermore, mining activities beneath the mountain can not only disrupt the integrity of the upper rock structures but also trigger significant fissures and ground collapses at the mountain's summit. This further exacerbates water erosion from karst pipelines, resulting in a high-risk area for geological hazards.

Figure 11a displays a 3-D representation of the subsidence zone and sliding slope induced by mining activities. The upper layer represents the original displacement field, while the middle and lower layers represent the mining effect and residual slope displacement, respectively. In addition, the topography of mountain FH is extracted through the profile P-Q and overlaid with the displacement rate, as shown in Figure 11b. The boundaries of exposed strata and the position of the underground coal seam are also labeled. According to the displacement profile depicted in Figure 11b with red dots, the surface displacement demonstrates a steady state along both sides of the P-Q profile. The selected profile range sufficiently captures the displacement trends for both positive and negative values. Thus, the chosen profile lines can effectively represent the characteristics of displacement.

Two areas of the slope present significant displacement, as indicated by the two positive peaks (Peak 1 and Peak 2) of the profile P-Q. The position of the Peak 1 is near the broken zone of the cliff and Peak 2 is located in the middle part of the slope. This phenomenon is similar to the findings of previous studies involving physical tests [27,51] and numerical simulations [30] of mining landslides, which exhibit similar mining conditions and geological structures. The downward propagation of cracks at the summit can cause the middle portion of the slope to become a compression-shear stress zone [27]. This fragile stress zone will be squeezed out due to tensile shearing, particularly during the rainy season, leading to a potential slip surface and an increased risk of landslides [30,51].

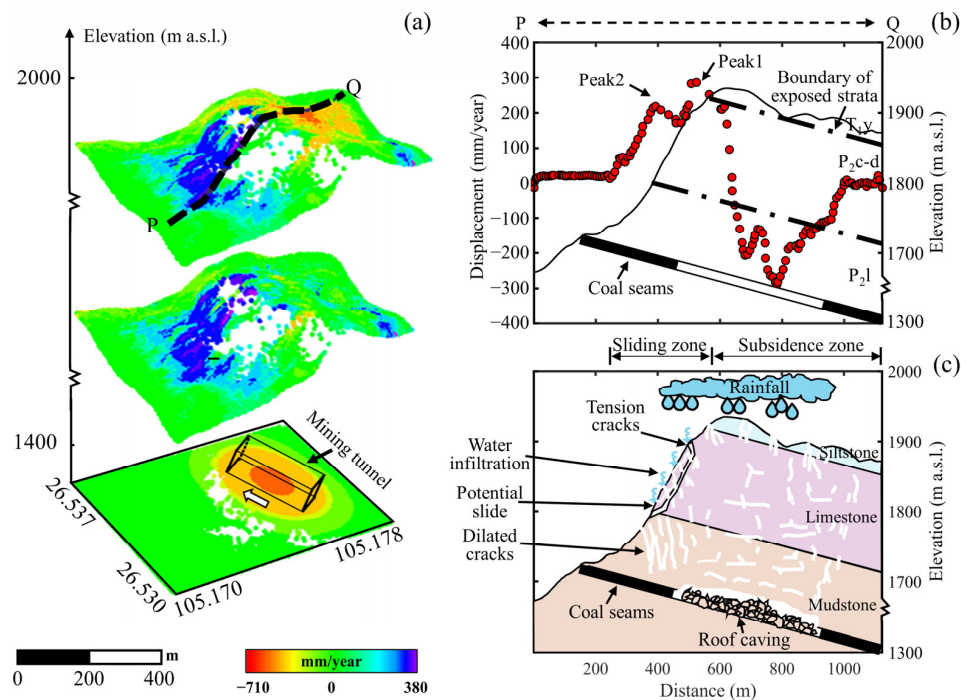


Figure 11. Deformation process of Tengqing landslides. (a) 3-D view of the mining-induced subsidence and sliding slope. (b) Displacement and topography profile along P-Q. (c) Schematic diagram illustrating the formation of Tengqing landslides.

Based on the aforementioned discussion and the related research, as the schematic diagrams show in Figure 11c, the formation of Tengqing landslides is summarized as the following stages: (1) Weathering and erosion: The top of the karst mountain is often composed of limestone, which is vulnerable to cracking due to weathering and rainfall erosion. (2) Mining subsidence: The excavation of underground coal seams directly causes numerous rock fractures above the working face and leads to surface sinking at the summit. Non-uniform horizontal displacement also results in the development and expansion of cracks. (3) Rock avalanche: As coal seams are repeatedly extracted, the unstable zone of the cliff may break away from the fractured rock layer, forming dangerous rock avalanches. The expansion of the underground working face will enlarge the broken areas of the mountain and increase the number of unstable slopes. (4) Potential landslide: Heavy rainfall can infiltrate into the cracks on the slope surface, increasing the water forces acting on the slope, leading to the further expansion of tensile cracks and accelerating slope displacement. Ultimately, this process can activate potential landslides.

6. Conclusions

This study monitored the ground displacement with large gradients caused by repeated underground mining, explored the kinematic process, and analyzed the mining and rainfall effects on ground displacement in both temporal and spatial domains. The SAR phase and offset information were fused to recover the large-gradient surface displacement. In the temporal domain, the multi-segment logistic model was proposed to split the temporal effects of mining and rainfall. In the spatial domain, the SPIM was utilized to invert the mining parameters and separate the mining subsidence and landslide displacement. The instability process of Tengqing landslides was mainly controlled by the combined effects of mining subsidence and rainfall, leading to ground collapse, tension cracks, rock avalanches, and potential compression shear failure in the different locations of the slope. This study can contribute to a better understanding of the kinematic process involved in repeated-mining induced landslides and provide valuable insights into the formation mechanism of mining-induced landslides under similar geological conditions.

Author Contributions: Conceptualization, H.C. and C.Z.; methodology, H.C.; validation, H.C. and C.Y.; investigation, H.C., C.Y., L.C. and Y.Z.; data curation, L.C. and C.Y.; writing—original draft preparation, H.C.; writing—review and editing, H.C., C.Z. and R.T.; visualization, H.C. and R.T.; supervision, C.Y., C.Z. and R.T.; funding acquisition, C.Z. and R.T. All authors have read and agreed to the published version of the manuscript.

Funding: This research was funded by the National Natural Science Foundation of China (Grant No. 41929001), the National Key R&D Program of China (No.2022YFC3004302), the Conselleria de Innovación, Universidades, Ciencia y Sociedad Digital in the framework of the project CIAICO/2021/335, the ESA-MOST China DRAGON-5 project (Ref. 59339), and the Chinese Scholarship Council studentship awarded (Ref. 202106560011).

Data Availability Statement: We thank JAXA for providing the ALOS/PALSAR-2 images of our study area. The SRTM DEM datasets were freely downloaded from <https://earthexplorer.usgs.gov/> (accessed on 18 February 2018), the GPM datasets were freely download from <https://gpm.nasa.gov/data/directory> (accessed on 8 August 2018), and the optical images were acquired from Google Earth and China Map-World.

Acknowledgments: We are grateful to the professional comments and suggestions provided by editor of the journal and the three anonymous reviewers.

Conflicts of Interest: The authors declare no conflict of interest.

References

1. Yin, Y.; Sun, P.; Zhang, M.; Li, B. Mechanism on Apparent Dip Sliding of Oblique Inclined Bedding Rockslide at Jiweishan, Chongqing, China. *Landslides* **2011**, *8*, 49–65. [[CrossRef](#)]
2. Zhao, C.; Zhang, Q.; Yin, Y.; Lu, Z.; Yang, C.; Zhu, W.; Li, B. Pre-, Co-, and Post-Rockslide Analysis with ALOS/PALSAR Imagery: A Case Study of the Jiweishan Rockslide, China. *Nat. Hazards Earth Syst. Sci.* **2013**, *13*, 2851–2861. [[CrossRef](#)]
3. Hibert, C.; Ekström, G.; Stark, C.P. Dynamics of the Bingham Canyon Mine Landslides from Seismic Signal Analysis. *Geophys. Res. Lett.* **2014**, *41*, 4535–4541. [[CrossRef](#)]
4. Williams, C.; Ross, B.; Zebker, M.; Leighton, J.; Gaida, M.; Morkeh, J.; Robotham, M. Assessment of the Available Historic RADARSAT-2 Synthetic Aperture Radar Data Prior to the Manefay Slide at the Bingham Canyon Mine Using Modern InSAR Techniques. *Rock. Mech. Rock. Eng.* **2021**, *54*, 3469–3489. [[CrossRef](#)]
5. Fan, X.; Xu, Q.; Scaringi, G.; Zheng, G.; Huang, R.; Dai, L.; Ju, Y. The “Long” Runout Rock Avalanche in Pusa, China, on August 28, 2017: A Preliminary Report. *Landslides* **2019**, *16*, 139–154. [[CrossRef](#)]
6. Lin, Y.N.; Park, E.; Wang, Y.; Quek, Y.P.; Lim, J.; Alcantara, E.; Loc, H.H. The 2020 Hpakant Jade Mine Disaster, Myanmar: A Multi-Sensor Investigation for Slope Failure. *ISPRS J. Photogramm. Remote Sens.* **2021**, *177*, 291–305. [[CrossRef](#)]
7. Hanssen, R.F. *Radar Interferometry: Data Interpretation and Error Analysis (Remote Sens. and Digital Image Processing)*; Springer: Berlin/Heidelberg, Germany, 2001.
8. Tomás, R.; Li, Z. Earth Observations for Geohazards: Present and Future Challenges. *Remote Sens.* **2017**, *9*, 194. [[CrossRef](#)]
9. Ferretti, A.; Fumagalli, A.; Novali, F.; Prati, C.; Rocca, F.; Rucci, A. A New Algorithm for Processing Interferometric Data-Stacks: SqueezSAR. *IEEE Trans. Geosci. Remote Sens.* **2011**, *49*, 3460–3470. [[CrossRef](#)]
10. Hooper, A. A Multi-Temporal InSAR Method Incorporating Both Persistent Scatterer and Small Baseline Approaches. *Geophys. Res. Lett.* **2008**, *35*, L16302. [[CrossRef](#)]
11. Berardino, P.; Fornaro, G.; Lanari, R.; Sansosti, E. A New Algorithm for Surface Deformation Monitoring Based on Small Baseline Differential SAR Interferograms. *IEEE Trans. Geosci. Remote Sens.* **2002**, *40*, 2375–2383. [[CrossRef](#)]
12. Dong, J.; Zhang, L.; Tang, M.; Liao, M.; Xu, Q.; Gong, J.; Ao, M. Mapping Landslide Surface Displacements with Time Series SAR Interferometry by Combining Persistent and Distributed Scatterers: A Case Study of Jiaju Landslide in Danba, China. *Remote Sens. Environ.* **2018**, *205*, 180–198. [[CrossRef](#)]
13. Shi, X.; Jiang, L.; Jiang, H.; Wang, X.; Xu, J. Geohazards Analysis of the Litang–Batang Section of Sichuan–Tibet Railway Using SAR Interferometry. *IEEE J. Sel. Top. Appl. Earth Obs. Remote Sens.* **2021**, *14*, 11998–12006. [[CrossRef](#)]
14. Modeste, G.; Doubre, C.; Masson, F. Time Evolution of Mining-Related Residual Subsidence Monitored over a 24-Year Period Using InSAR in Southern Alsace, France. *Int. J. Appl. Earth Obs. Geoinf.* **2021**, *102*, 102392. [[CrossRef](#)]
15. Casagli, N.; Intrieri, E.; Tofani, V.; Gigli, G.; Raspin, F. Landslide Detection, Monitoring and Prediction with Remote-Sensing Techniques. *Nat. Rev. Earth Environ.* **2023**, *4*, 51–64. [[CrossRef](#)]
16. Nefros, C.; Alatza, S.; Loupasakis, C.; Kontoes, C. Persistent Scatterer Interferometry (PSI) Technique for the Identification and Monitoring of Critical Landslide Areas in a Regional and Mountainous Road Network. *Remote Sens.* **2023**, *15*, 1550. [[CrossRef](#)]
17. Hu, J.; Yu, Y.; Gui, R.; Zheng, W.; Guo, A. Spatial Distribution Analysis of Landslide Deformations and Land-Use Changes in the Three Gorges Reservoir Area by Using Interferometric and Polarimetric SAR. *Remote Sens.* **2023**, *15*, 2302. [[CrossRef](#)]

18. Cai, J.; Liu, G.; Jia, H.; Zhang, B.; Wu, R.; Fu, Y.; Xiang, W.; Mao, W.; Wang, X.; Zhang, R. A New Algorithm for Landslide Dynamic Monitoring with High Temporal Resolution by Kalman Filter Integration of Multiplatform Time-Series InSAR Processing. *Int. J. Appl. Earth Obs. Geoinf.* **2022**, *110*, 102812. [[CrossRef](#)]
19. Wang, B.; Zhao, C.; Zhang, Q.; Liu, X.; Lu, Z.; Liu, C.; Zhang, J. Sequential DS-ISBAS InSAR Deformation Parameter Dynamic Estimation and Quality Evaluation. *Remote Sens.* **2023**, *15*, 2097. [[CrossRef](#)]
20. Baran, I.; Stewart, M.; Claessens, S. A New Functional Model for Determining Minimum and Maximum Detectable Deformation Gradient Resolved by Satellite Radar Interferometry. *IEEE Trans. Geosci. Remote Sens.* **2005**, *43*, 675–682. [[CrossRef](#)]
21. Strozzi, T.; Luckman, A.; Murray, T.; Wegmüller, U.; Werner, C.L. Glacier Motion Estimation Using SAR Offset-Tracking Procedures. *IEEE Trans. Geosci. Remote Sens.* **2002**, *40*, 2384–2391. [[CrossRef](#)]
22. Casu, F.; Manconi, A.; Pepe, A.; Lanari, R. Deformation Time-Series Generation in Areas Characterized by Large Displacement Dynamics: The SAR Amplitude Pixel-Offset SBAS Technique. *IEEE Trans. Geosci. Remote Sens.* **2011**, *49*, 2752–2763. [[CrossRef](#)]
23. Zhao, C.; Lu, Z.; Zhang, Q. Time-Series Deformation Monitoring over Mining Regions with SAR Intensity-Based Offset Measurements. *Remote Sens. Lett.* **2013**, *4*, 436–445. [[CrossRef](#)]
24. Fan, H.; Gao, X.; Yang, J.; Deng, K.; Yu, Y. Monitoring Mining Subsidence Using A Combination of Phase-Stacking and Offset-Tracking Methods. *Remote Sens.* **2015**, *7*, 9166–9183. [[CrossRef](#)]
25. Wang, L.; Deng, K.; Zheng, M. Research on Ground Deformation Monitoring Method in Mining Areas Using the Probability Integral Model Fusion D-InSAR, Sub-Band InSAR and Offset-Tracking. *Int. J. Appl. Earth Obs. Geoinf.* **2020**, *85*, 101981. [[CrossRef](#)]
26. Ghabraie, B.; Ren, G.; Barbato, J.; Smith, J.V. A Predictive Methodology for Multi-Seam Mining Induced Subsidence. *Int. J. Rock Mech. Min. Sci.* **2017**, *93*, 280–294. [[CrossRef](#)]
27. Yang, Z.; Zhao, Q.; Liu, X.; Yin, Z.; Zhao, Y.; Li, X. Experimental Study on the Movement and Failure Characteristics of Karst Mountain with Deep and Large Fissures Induced by Coal Seam Mining. *Rock. Mech. Rock. Eng.* **2022**, *55*, 4839–4867. [[CrossRef](#)]
28. Fang, K.; Miao, M.; Tang, H.; Jia, S.; Dong, A.; An, P.; Zhang, B. Insights into the Deformation and Failure Characteristic of a Slope Due to Excavation through Multi-Field Monitoring: A Model Test. *Acta Geotech.* **2023**, *18*, 1001–1024. [[CrossRef](#)]
29. Salmi, E.F.; Nazem, M.; Karakus, M. Numerical Analysis of a Large Landslide Induced by Coal Mining Subsidence. *Eng. Geol.* **2017**, *217*, 141–152. [[CrossRef](#)]
30. Li, J.; Li, B.; He, K.; Gao, Y.; Wan, J.; Wu, W.; Zhang, H. Failure Mechanism Analysis of Mining-Induced Landslide Based on Geophysical Investigation and Numerical Modelling Using Distinct Element Method. *Remote Sens.* **2022**, *14*, 6071. [[CrossRef](#)]
31. Jarosz, A.; Karmis, M.; Sroka, A. Subsidence Development with Time-Experiences from Longwall Operations in the Appalachian Coalfield. *Int. J. Min. Geol. Eng.* **1990**, *8*, 261–273. [[CrossRef](#)]
32. Yang, Z.; Li, Z.; Zhu, J.; Yi, H.; Hu, J.; Feng, G. Deriving Dynamic Subsidence of Coal Mining Areas Using InSAR and Logistic Model. *Remote Sens.* **2017**, *9*, 125. [[CrossRef](#)]
33. Yang, D.; Qiu, H.; Ma, S.; Liu, Z.; Du, C.; Zhu, Y.; Cao, M. Slow Surface Subsidence and Its Impact on Shallow Loess Landslides in a Coal Mining Area. *CATENA* **2022**, *209*, 105830. [[CrossRef](#)]
34. Chen, H.; Zhao, C.; Li, B.; Gao, Y.; Chen, L.; Liu, D. Monitoring Spatiotemporal Evolution of Kaiyang Landslides Induced by Phosphate Mining Using Distributed Scatterers InSAR Technique. *Landslides* **2023**, *20*, 695–706. [[CrossRef](#)]
35. Chen, L.; Zhao, C.; Li, B.; He, K.; Ren, C.; Liu, X.; Liu, D. Deformation Monitoring and Failure Mode Research of Mining-Induced Jianshanying Landslide in Karst Mountain Area, China with ALOS/PALSAR-2 Images. *Landslides* **2021**, *18*, 2739–2750. [[CrossRef](#)]
36. Yan, W.; Chen, J.; Yang, W.; Liu, X.; Wang, W.; Zhang, W. On-Site Measurement on Surface Disturbance Law of Repeated Mining with High Relief Terrain. *Sustainability* **2022**, *14*, 3166. [[CrossRef](#)]
37. Wang, N.; Zhong, Z.; Liu, X.; Gao, G. Failure Mechanism of Anti-Inclined Karst Slope Induced by Underground Multiseam Mining. *Geofluids* **2022**, *2022*, 1302861. [[CrossRef](#)]
38. Lu, Z.; Dzurisin, D.; Biggs, J.; Wicks, C.; McNutt, S. Ground Surface Deformation Patterns, Magma Supply, and Magma Storage at Okmok Volcano, Alaska, from InSAR Analysis: 1. Intereruption Deformation, 1997–2008. *J. Geophys. Res.* **2010**, *115*, B00B02. [[CrossRef](#)]
39. Wright, T.; Fielding, E.; Parsons, B. Triggered Slip: Observations of the 17 August 1999 Izmit (Turkey) Earthquake Using Radar Interferometry. *Geophys. Res. Lett.* **2001**, *28*, 1079–1082. [[CrossRef](#)]
40. Kim, J.-W.; Lu, Z.; Degrandpre, K. Ongoing Deformation of Sinkholes in Wink, Texas, Observed by Time-Series Sentinel-1A SAR Interferometry (Preliminary Results). *Remote Sens.* **2016**, *8*, 313. [[CrossRef](#)]
41. Litwiniszyn, J. The Theories and Model Research of Movements of Ground Masses. In Proceedings of the European Congress on Ground Movement, Leeds, UK, 9–12 April 1957; Volume 202, p. 209.
42. Liu, B.; Liao, G. *Basic Law of Surface Movement in Coal Mine*; China Coal Industry Press: Beijing, China, 1965.
43. Yang, Z.; Li, Z.; Zhu, J.; Yi, H.; Feng, G.; Hu, J.; Wu, L.; Preusse, A.; Wang, Y.; Papst, M. Locating and Defining Underground Goaf Caused by Coal Mining from Space-Borne SAR Interferometry. *ISPRS J. Photogramm. Remote Sens.* **2018**, *135*, 112–126. [[CrossRef](#)]
44. Du, S.; Wang, Y.; Zheng, M.; Zhou, D.; Xia, Y. Goaf Locating Based on InSAR and Probability Integration Method. *Remote Sens.* **2019**, *11*, 812. [[CrossRef](#)]
45. Scambos, T.A.; Dutkiewicz, M.J.; Wilson, J.C.; Bindschadler, R.A. Application of Image Cross-Correlation to the Measurement of Glacier Velocity Using Satellite Image Data. *Remote Sens. Environ.* **1992**, *42*, 177–186. [[CrossRef](#)]
46. MathWorks Findpeaks Function Documentation. *MATLAB Help Center*, R2021b ed.; MathWorks: Natick, MA, USA, 2021.

47. Schlägel, R.; Doubre, C.; Malet, J.P.; Masson, F. Landslide Deformation Monitoring with ALOS/PALSAR Imagery: A D-InSAR Geomorphological Interpretation Method. *Geomorphology* **2015**, *231*, 314–330. [[CrossRef](#)]
48. Meng, Q.; Confuorto, P.; Peng, Y.; Raspini, F.; Bianchini, S.; Han, S.; Liu, H.; Casagli, N. Regional Recognition and Classification of Active Loess Landslides Using Two-Dimensional Deformation Derived from Sentinel-1 Interferometric Radar Data. *Remote Sens.* **2020**, *12*, 1541. [[CrossRef](#)]
49. Liu, X.; Zhao, C.; Zhang, Q.; Yang, C.; Zhu, W. Heifangtai Loess Landslide Type and Failure Mode Analysis with Ascending and Descending Spot-Mode TerraSAR-X Datasets. *Landslides* **2020**, *17*, 205–215. [[CrossRef](#)]
50. Chen, H.; Zhao, C.; Sun, R.; Chen, L.; Wang, B.; Li, B. Two-Dimensional Deformation Monitoring of Karst Landslides in Zongling, China, with Multi-Platform Distributed Scatterer InSAR Technique. *Landslides* **2022**, *19*, 1767–1777. [[CrossRef](#)]
51. Xiong, S.; Shi, W.; Wang, Y.; Zhu, C.; Yu, X. Deformation and Failure Process of Slope Caused by Underground Mining: A Case Study of Pusa Collapse in Nayong County, Guizhou Province, China. *Geofluids* **2022**, *2022*, 1592703. [[CrossRef](#)]

Disclaimer/Publisher’s Note: The statements, opinions and data contained in all publications are solely those of the individual author(s) and contributor(s) and not of MDPI and/or the editor(s). MDPI and/or the editor(s) disclaim responsibility for any injury to people or property resulting from any ideas, methods, instructions or products referred to in the content.